

Simulation of Particle Transport in Electrostatic Precipitators

Leif Lind and Niels F. Nielsen
FLS Airtech A/S
DK-2500 Valby
Denmark

Poul S. Larsen
Department of Mechanical Engineering, Fluid Mechanics Section,
Technical University of Denmark, Building 403, DK-2800 Kgs. Lyngby, Denmark

Elisabeth Akoh Hove
FORCE Technology, DK-2800 Kgs. Lyngby, Denmark

Abstract

Simulation models for sizing of ElectroStatic Precipitators (ESPs) have been developed for the last 15 to 20 years, but only a few models take into account all physical processes involved, i.e. electric field, particle space charge, dust resistivity, particle concentration field, and flow field, and most models are confined to two dimensions.

A new extended FLS-Airtech-model simulates most physical processes in an ESP and is fully three-dimensional. The model has been implemented in a commercial Computational Fluid Dynamics (CFD) code in order to obtain a high degree of flexibility and generality and an efficient visualization tool for the model output data.

The presented results include validation of the extended model against pilot and full scale ESP data. Further, simulations based on a typical FLS Airtech ESP geometry with spike discharge electrodes are presented. Focus is on model results and on discussions of different parameters important for optimal operation of ESPs, e.g. current density, secondary flows, turbulence, particle characteristics and charging. Most of these parameters are difficult or even impossible to measure in full scale or even in pilot ESPs.

1. Introduction

Numerical modelling of the precipitation process is challenging and many approaches have been made to model ElectroStatic Precipitators (ESPs) (Anagnostopoulos & Bergeles, 2002, Arrondel et al., 2001, Egli et al., 1996, Houlgreave et al., 1996, Lawless, 1996, Medlin et al., 1998, Meroth et al., 1996, Parasram & Taylor, 2001, Schmid & Buggisch, 1998, Schmitz et al., 2001, Zamany, 1992, 1995a). The literature contains models with different complexity but many are two-dimensional. The motivation for model development comes from the need to predict the complex electro-hydrodynamic flow and from an industrial point of view from the need to improve efficiency of the ESP design.

The electrical conditions in an ESP are influenced by internal structural elements, the imposed electric potential, the induced ionic and particle space charge, the mobility of the gas, and the dust resistivity. The interaction of these parameters leads to an electrical balance in the system that dominates the precipitation process. In prediction and optimisation of the ESP performance the knowledge of this balance is therefore of major importance. On the other hand the electrostatic field and the induced charge density impose distortion of the uniform flow field, which results in secondary flows. The secondary flow forms axial rolls and generate turbulence (Thomsen, 1982, Zamany, 1992). Hence the fundamental physics of the ESP process also requires three-dimensional modelling of the turbulent flow field.

In the present study the numerical model solves the three-dimensional electrical and turbulent flow field and concentration of different particle classes. The most important interactions between the different fields are included in the model and sketched by the arrows in Figure 1. The electrical force is the main mechanism in the precipitator process and the three-dimensional model of Zamany (1992) is used to calculate the electrical conditions influenced by ionic and particle space charge. This model solves simultaneously the coupled electric and current density fields. The electric field takes into account the influence of ionic convection and diffusion due to corona discharge, the presence of particle space charge (electric field distortion) and the effect of dust resistivity at the collector plates.

The weak interaction from the flow field on the electric field is not included. The flow field influenced by the electrical field (body force) and the actual geometry is solved in order to take into account induced secondary flows. The weak interaction from the particle field on the flow field is not included. The turbulent particle transport controlled by both the electric field (particle charging) and the flow field (fluid particle dynamics) is modelled by an Eulerian approach due to the highly coupled problem. Furthermore, low computational effort is obtained by treating the particles as a second continuum phase characterized by its concentration.

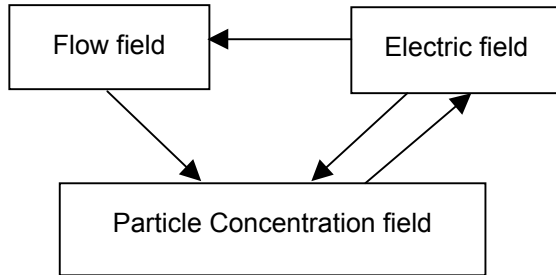


Figure 1. Interaction between different components of the ESP simulation model.

The presented model is an extension of the FLS Airtech ESP simulation model by introduction of a three-dimensional flow field. The model is validated against pilot as well as full-scale ESP data. Further results of different model applications and different electrodes of a typical ESP are given and discussed.

2. The numerical model

The new FLS Airtech ESP simulation model is fully three-dimensional and implemented in a commercial CFD code STAR-CD. The basics of the CFD code – the flow field and the particle concentration field – have been supplemented with additional parts for calculating the electrical field and the charging mechanism by including the model of Zamany (1992) as user sub routines.

2.1. Model description

This section describes the background for the numerical analysis including model description and modelling procedure. Only the basic principles are described and for a more detailed discussion of the ESP model is referred to (Akoh and Nielsen, 2000, STAR-CD manual, 2002, and Zamany, 1992 & 1995a,b).

The three-dimensional electrostatic field between discharge electrode and collector plate in terms of potential and charge density is computed by solving

$$(1) \quad \nabla \cdot \mathbf{E} = (\rho_i + \rho_p) / \epsilon_0, \quad \nabla \cdot \mathbf{J} = 0, \quad \text{where} \quad \mathbf{J} = (\rho_i b_i \mathbf{E} - D_i \nabla \rho_i) + (\rho_p b_p \mathbf{E} - D_p \nabla \rho_p).$$

$\mathbf{E} = -\nabla \phi$ is the electric field, ϕ the electric potential, ρ_i the space charge density of gas ions, ρ_p the particle space charge density, ϵ_0 the electric permittivity, \mathbf{J} the current density, b_i the mobility of gas ions, b_p the mobility of the particles, and D_i and D_p ion and particle diffusivity coefficients, respectively. For further details of modelling procedure and coefficient values is referred to Zamany (1992 & 1995b).

The three-dimensional turbulent gas flow field is computed within the environment of STAR-CD. The flow field is governed by the Navier-Stokes equations, which are solved together with equations for mass conservation. Turbulence is modelled by the standard $k-\epsilon$ model (Launder & Spalding, 1974), which is widely used for industrial internal flows and comprises differential transport equations for the turbulent kinetic energy k and its dissipation rate ϵ . The high Reynolds number form is used in conjunction with the so-called “law of the wall” representation of the boundary layer flow. This choice is based on the best compromise between accuracy and boundary layer resolution. The body force from the influence of the electric field, $\mathbf{F}_e = \rho_i \mathbf{E}$, is added as source term in the momentum equations. For further details of modelling the turbulent flow field is referred to Feriger & Peric (1996), STAR-CD manual (2002), and Wilcox (1993).

The concentration field (particle motion) is computed within the STAR-CD environment as an Euler formulation. The particles are divided into d_i classes each having concentration c_i (n_i scalar equations). The transport equation for c_i includes influence from the electric field by a source terms $-\nabla \cdot (c_i \mathbf{v}_e)$, \mathbf{v}_e denoting the electric drift velocity. The influence from the flow field is included in particle drift velocity,

$\mathbf{v}_p = \mathbf{v}_f + \mathbf{v}_e$, \mathbf{v}_f denoting the gas flow velocity. The particle mass flux deposited on the collecting plates is calculated as $\Delta \dot{m}_{\text{dust}} = \int_A \mathbf{v}_p \cdot \mathbf{n} dA$, where \mathbf{n} is the outward normal to the cell flux area A .

2.2. Geometry, computational mesh and boundary conditions

The ESP geometry of the present study is shown in Figure 2. The figure shows one field with one set of parallel collecting plates and a series of electrodes. The flow is from left to right (axial flow between parallel collecting plates). The simulation model is based on a cell model for the electric field and a section model for the flow and concentration fields. Thus, based on the strategy of Zamany (1992) the electric field is solved on a so-called "unit" cell geometry. The unit cell is defined as a small symmetrical calculation volume between two electrodes in the axial direction and between one collector plate and the electrode symmetry line in the transversal direction (see Figure 2). The flow field and the particle concentration field are solved on a so-called "section" model geometry due to the elliptic nature of the three-dimensional flow field. A section model is defined as the calculation domain represented by the length of one electrical field in the axial direction and as the distance between one collector plate and the electrode symmetry line in the transversal direction (i.e. several unit cells). The height of the unit cell as well as of the section model is arbitrary and depends on the distance between the pins of the electrodes. The unit cell/section model strategy requires interpolation of the electrostatic field to the flow field and particle concentration field (unit cell to section model geometry).

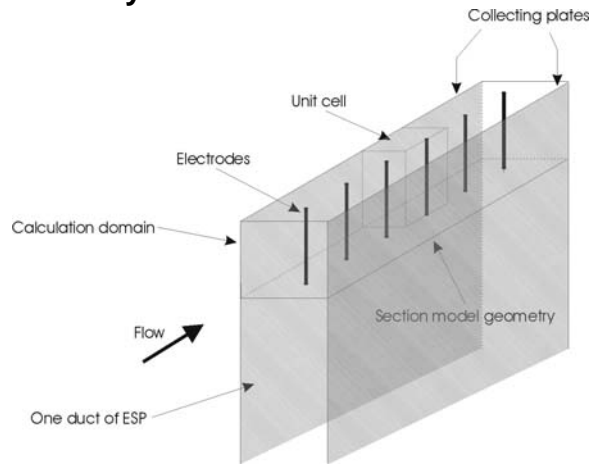


Figure 2. Computational domain with electrodes.

The computational mesh consists of a Cartesian mesh structure with cubic cells of any size. The local mesh refinement included in STAR-CD is not included and the actual geometry of the electrodes is not modelled.

The boundaries of the cell model consists of inlet at left, outlet at right, wall at collector plate, symmetry line at electrodes center line, and symmetry line at top and bottom. The boundary conditions for the electric field are: $\partial/\partial\mathbf{n} = \mathbf{0}$ at symmetry planes, $\varphi = 0$ and $\rho_i = 0$ at the collector plate, $\varphi = \varphi_0$ at the electrode, and $\rho_i = \rho_0$ at corona points, the latter being adjusted iteratively until the calculated mean current density J_m at the collector plate equals the wanted value for the specified electrode potential φ_0 (Zamany, 1995a). The boundary conditions of the section model for the flow field are: $\partial/\partial\mathbf{n} = \mathbf{0}$ at symmetry planes, no-slip at the collector plate (wall), at the inlet a uniform velocity profile is specified, and at the outlet the exit mass flow is fixed from overall continuity considerations. The boundary conditions of the section model for the particle concentration field are: uniform concentration at inlet, $\partial/\partial\mathbf{n} = 0$ at the outlet, at collector plate (zero slope), and at symmetry lines (zero flux).

2.3. Model approximations

The main purpose of the present study is accurate modelling of the precipitation process in an ESP, while mechanical operations like rapping etc. are not included.

The global concept of modelling a full ESP is usually applied to gas flow modelling. In the present case the local concept of modelling the precipitation process between one set of parallel collecting plates is applied. This means that the basic assumptions are uniform gas velocity and particle concentration at the inlet to each field in the full (global) ESP. So far this approach is a necessary assumption in order to keep the number of computational cells and by that, the computational time at a reasonable level.

3. Results and discussions

Three different cases have been considered, that of a pilot and a full-scale ESP with different electrodes and operating conditions used for validation purposes (section 3.1), that of a pilot ESP set-up used for model applications with focus on parameters important for optimal ESP operation (section 3.2), and finally that of modelling and evaluating different electrodes (section 3.3).

3.1. Case 1 - Model validation

Two model validation cases have been investigated, that of a pilot ESP with low inlet dust load and fine particle sizes and that of a full-scale ESP with low inlet dust load and coarse dust particles sizes.

Pilot ESP case

The pilot ESP is a two-field-one-duct precipitator with an inlet transition piece, flat dust hoppers, and an outlet cone. The first field has a duct width of 300 mm and the second field a duct width of 500 mm. The length of each field is 1.8 m, the height 1.5 m, and the 2 times 6 collecting plates (300 mm length) of each field are plane. In order to avoid sneackage in such small fields with a nominal height of 1.5 m baffles have been placed at the top, bottom, and between plate curtains and compartment walls. Investigations have shown that sneackage is not a problem.

Test simulations are carried out for four different electrodes as shown in Table 1 and Figure 3. Note that the difference between AES-A-76-0 and AES-B-76-0 is that the pins are staggered as in left Figure 3 and placed opposite to each other (non-staggered), respectively. The pins of AES-A-76-0, AES-B-76-0, and Fibulax-100-0 point in the axial flow direction while pins of AES-76-90 point towards the collector plates.

| Electrode Type | body diam. (mm) | pin diam./length (mm) | pin spacing along electrode and orientation relative to axial |
|----------------|-----------------|-----------------------|---|
| AES-A-76-0 | 25 | 1.5 / 12.7 | 76 mm staggered, $\pm 0^\circ$ (pointing axially) |
| AES-B-76-0 | 25 | 1.5 / 12.7 | 76 mm non-staggered, $\pm 0^\circ$ (pointing axially) |
| AES-76-90 | 25 | 1.5 / 12.7 | 76 mm staggered, $\pm 90^\circ$ to axial |
| Fibulax-100-0 | 35 | 2.5 / 25 | 100 mm staggered, $\pm 0^\circ$ (pointing axially) |

Table 1. Four types of electrodes used for test simulations.

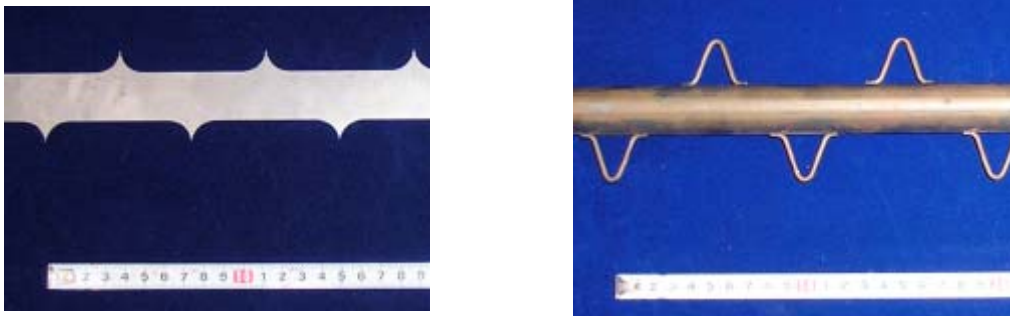


Figure 3. Photos of two types of electrodes used for test simulations. Left AES-A-76-0 type and right Fibulax-100-0 type.

The input data for the ESP simulation model are shown in Table 2. The corona start potential for AES type electrodes are 17 kV and for Fibulax type electrodes 38 kV. Note that the mean particle diameter is relatively small and that the resistivity is relatively low.

Measured and calculated current-voltage characteristics (CVCs) for clean and dust loaded pilot ESP with AES-A-76-0 and AES-B-76-0 electrodes are shown in left and right Figures 4, respectively. Only the results of field 1 are presented in this case.

In the clean pilot ESP, computed CVCs are in good agreement with measured values. The deviations at low current densities ($< 0.03 \text{ mA/m}^2$) are ascribed to uncertainties of the measurements because it is difficult to measure at these low current values while the small deviations at high current densities ($> 0.4 \text{ mA/m}^2$) are ascribed to uncertainties of the true collector plate area of the measurements. Further note that computed AES-A-76-0 and AES-B-76-0 CVCs show exactly identical results. But staggered and non-staggered pin electrodes may still have different current density at the collecting plate.

| CASE | FLS Airtech Pilot ESP | |
|---|-----------------------|----------|
| Field No/plate spacing [mm]. | 1/300 | 2/500 |
| <u>Electrical conditions:</u> | | |
| Corona start potential, ϕ_0 , [kV] | 17/38 | 17/38 |
| Current density level [mA/m^2] | 0.01-1.0 | 0.01-1.0 |
| <u>Flow conditions:</u> | | |
| Mean bulk velocity V_0 [m/s] | 1.3 | 1.3 |
| Temperature [$^\circ\text{C}$] | 22 | 22 |
| ESP pressure [bar] | 1.0 | 1.0 |
| <u>Dust particle conditions:</u> | | |
| Particle mean diameter [μm] | 5.3 | - |
| Particle standard deviation [μm] | not log nor. | - |
| Number of particle classes | 30 | - |
| Particle mass density [kg/m^3] | 2700 | 2700 |
| Dust load [g/m^3] | 1.0 | - |
| Particle resistivity [Ωcm] | 10^8 | 10^8 |

Table 2. Pilot ESP input data for simulation model

In the loaded pilot ESP (field 1) with AES-B-76-0 electrodes measured and computed CVCs shows small deviation (right Figure 4) but still good agreement.

Calculations have shown that both clean and dust loaded cases with AES-76-90 and Fibulax-100-0 type electrodes give identical trends as described above for the AES-76-0 electrode. For the Fibulax-100-0 electrode see section “Full-scale ESP case” and Figure 5 below.

In Table 3 global parameters such as ESP efficiency and dust emission are compared in order to study the overall ESP performance. Measured and computed data are shown for three different electrodes of Table 1 at identical current density level of 0.22 mA/m^2 . AES-A-76-0 and AES-B-76-0 are considered as one electrode due to identical CVCs all through current density distributions may be different.

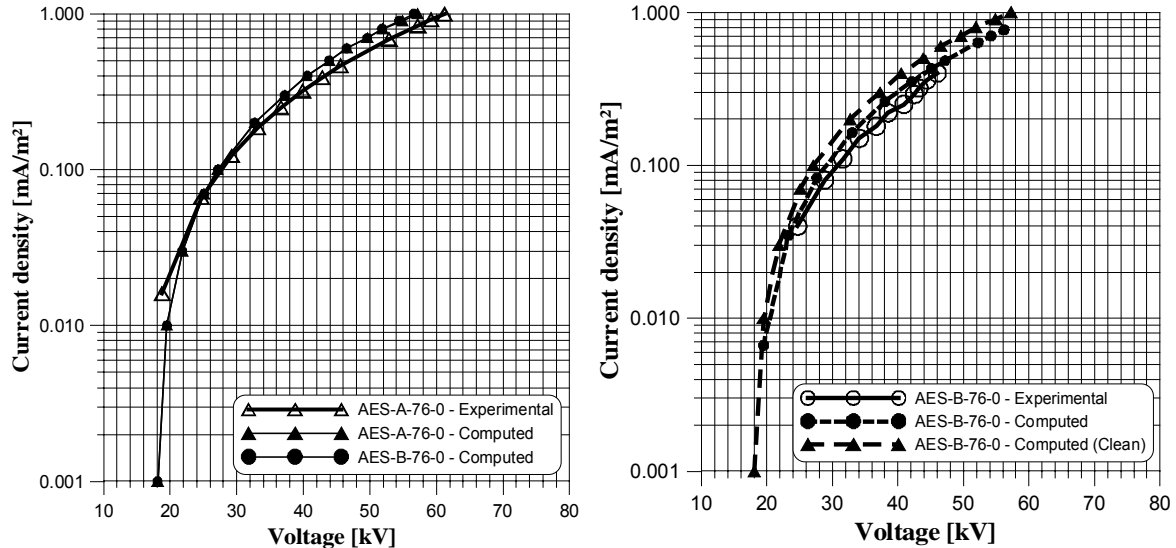


Figure 4. Measured and computed CVCs for clean (left) and dust loaded (right) pilot ESP.

There are quite large differences between measured and computed data with a clear indication of lower ESP efficiency for the simulation model. But the Fibulax-100-0 electrode gives the best performance and also the smallest deviation from measurements. Investigations have shown that the lower efficiency of the simulation model may be related to the small particle sizes (less than approximately $2.0 \mu\text{m}$) present in the pilot ESP case, which could be related to the charging model. The present ESP simulation model uses the charging model of Southern Research Institute (1975) including both field and diffusion charging. In conclusion, measured clean and loaded CVCs showed good agreement with computed data of the present simulation model. But quite large deviations in predicting the ESP efficiency of the pilot ESP case are observed and collecting efficiencies of small particle sizes needs further development. However, it should be noted that both measurements and simulations indicate that the electrode with the best ESP performance is the Fibulax-100-0.

| CASE | FLS Airtech Pilot ESP | |
|-----------------------------------|-----------------------|----------|
| Field No. 1 (AES-76-0) | Measured | computed |
| Operating voltage [kV] | 38.5 | 38.5 |
| Efficiency [%] | 98.6 | 91.6 |
| Dust emission [mg/m^3] | 13.7 | 84.4 |
| Field No. 1 (AES-76-90) | | |
| Operating voltage [kV] | 36.6 | 36.6 |
| Efficiency [%] | 97.4 | 84.3 |
| Dust emission [mg/m^3] | 24.9 | 157 |
| Field No. 1 (Fibulax-100-0) | | |
| Operating voltage [kV] | 58.0 | 58.0 |
| Efficiency [%] | 98.7 | 95.9 |
| Dust emission [mg/m^3] | 12.5 | 40.6 |

Table 3. Pilot ESP efficiency for three different electrodes

Full-scale ESP case

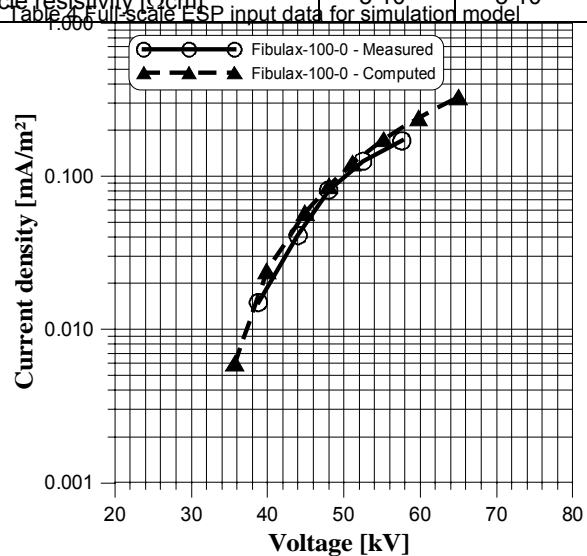
The full-scale validation test is performed on an FLS Airtech ESP operating on an incinerator plant. The full-scale ESP is a two-field precipitator with an FLS Airtech B-type inlet transition piece, dust hoppers, and a C-type outlet funnel. The first field has a length of 3.6 m and the second field a length of 5.4 m both with 400 mm duct width. The height is 6.5 m, the width 5.3 m, and each field is fitted with Fibulax-100-0 electrodes with a spacing

| CASE | Full-scale ESP | |
|-------------------------------------|----------------|----------|
| | Measured | computed |
| Field No. 1 – Fibulax-100-0 | | |
| Operating voltage [kV] | 58.0 | 58.0 |
| Efficiency [%] | - | 98.4 |
| Dust emission [mg/m ³] | - | 78 |
| Mean diameter outlet [μm] | - | 1.6 |
| Field No. 2 – Fibulax-100-0 | | |
| Operating voltage [kV] | 62.0 | 60.0 |
| Efficiency [%] | 99.7 | 99.8 |
| Dust emission [mg/Nm ³] | 17 | 11 |
| Mean diameter outlet [μm] | - | 1.3 |

of 450 mm. Other process parameters of the full-scale ESP are shown in Table 4. Note that the mean particle diameter is relatively high and that the resistivity is low.

The calculated and the measured field 1 CVC's for the dust loaded case are shown in Figure 5. As can be seen on the figure very good agreement between calculated and measured values is obtained. Further calculations have shown excellent agreement between measured and calculated data for field 2 as well. Table 5 shows ESP efficiency at the operating point of 0.21 and 0.33 mA/m² for field 1 and 2, respectively. In this case the ESP simulation model predicts the emission very well, which must be ascribed to the more easy case of collecting large particles. In conclusion the full-scale validation case shows excellent agreement between computed and field data and the simulation model can be used for investigating similar full-scale ESPs with relatively coarse dust.

| CASE | Full-scale ESP | |
|--|----------------|----------------|
| | 1 | 2 |
| Field No. | 1 | 2 |
| <u>Electrical conditions:</u> | | |
| Corona start potential, ϕ_0 , [kV] | 38 | 38 |
| Current density level [mA/m ²] | 0.01-0.33 | 0.01-0.4 |
| <u>Flow conditions:</u> | | |
| Mean bulk velocity V_0 [m/s] | 0.73 | 0.73 |
| Temperature [°C] | 165 | 165 |
| ESP pressure [mmWG] | -100 | -100 |
| <u>Dust particle conditions:</u> | | |
| Particle mean diameter [μm] | 23 | - |
| Particle standard deviation [μm] | 3.1 | - |
| Number of particle classes | 30 | - |
| Particle mass density [kg/m ³] | 1400 | 1400 |
| Dust load [g/m ³] | 5.0 | - |
| Particle resistivity [Ωcm] | $5 \cdot 10^7$ | $5 \cdot 10^7$ |



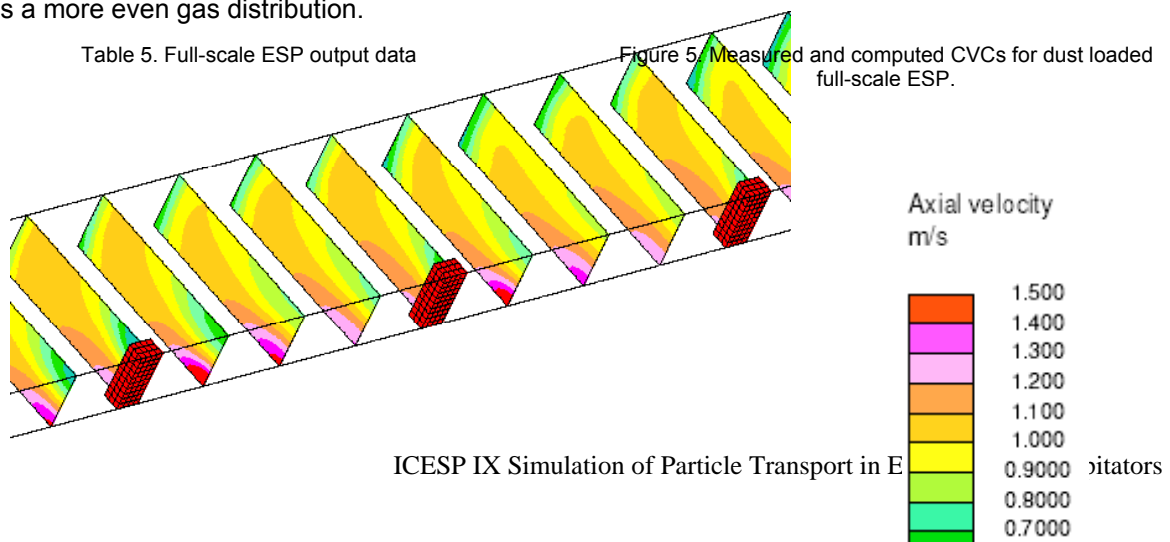
3.2. Case 2 – Model results for different electrodes (Fibulax-100-0 & AES-76-0)

This section deals with comparison of results for the staggered electrode Fibulax-100-0 and the non-staggered electrode AES-76-0. Notice that there is an emitter on the Fibulax-100-0 at the top and bottom symmetry plane, the upper one pointing upstream and the lower one pointing downstream. On the AES-76-0 there are two emitters at the bottom symmetry plane pointing upstream and downstream. All figures are presented inside the field model defined in Figure 2

In Figure 6, only showing the region between the second and fourth electrode, is shown the axial velocity distribution (u_x) for the Fibulax-100-0 electrode at 0.24 mA/m² and for the AES-76-0 electrode at 0.30 mA/m². The former creates a rather uneven velocity distribution across the duct while the latter gives a more even gas distribution.

Table 5. Full-scale ESP output data

Figure 5. Measured and computed CVCs for dust loaded full-scale ESP.



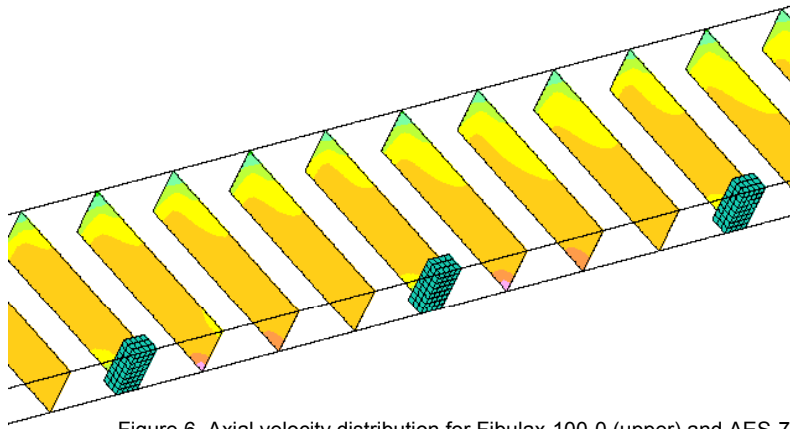


Figure 6. Axial velocity distribution for Fibulax-100-0 (upper) and AES-76-0 (lower) electrodes.

In Figure 7 the transverse concentration along the duct is seen as iso-colour plots. Notice that the staggered electrode, Fibulax-100-0, creates concentration profiles almost parallel to the collecting surface, collecting plate plane, implicitly demonstrating that there is a finite diffusivity giving concentration profiles closer to the laminar concept than to the Deutsch concept with infinite diffusivity. Contrary to this the non-staggered electrode, AES-76-0, especially at high current density, turns the concentration profiles towards a direction parallel with the top and bottom plane (symmetry planes), i.e. more like the concentration distribution of the Deutsch concept.

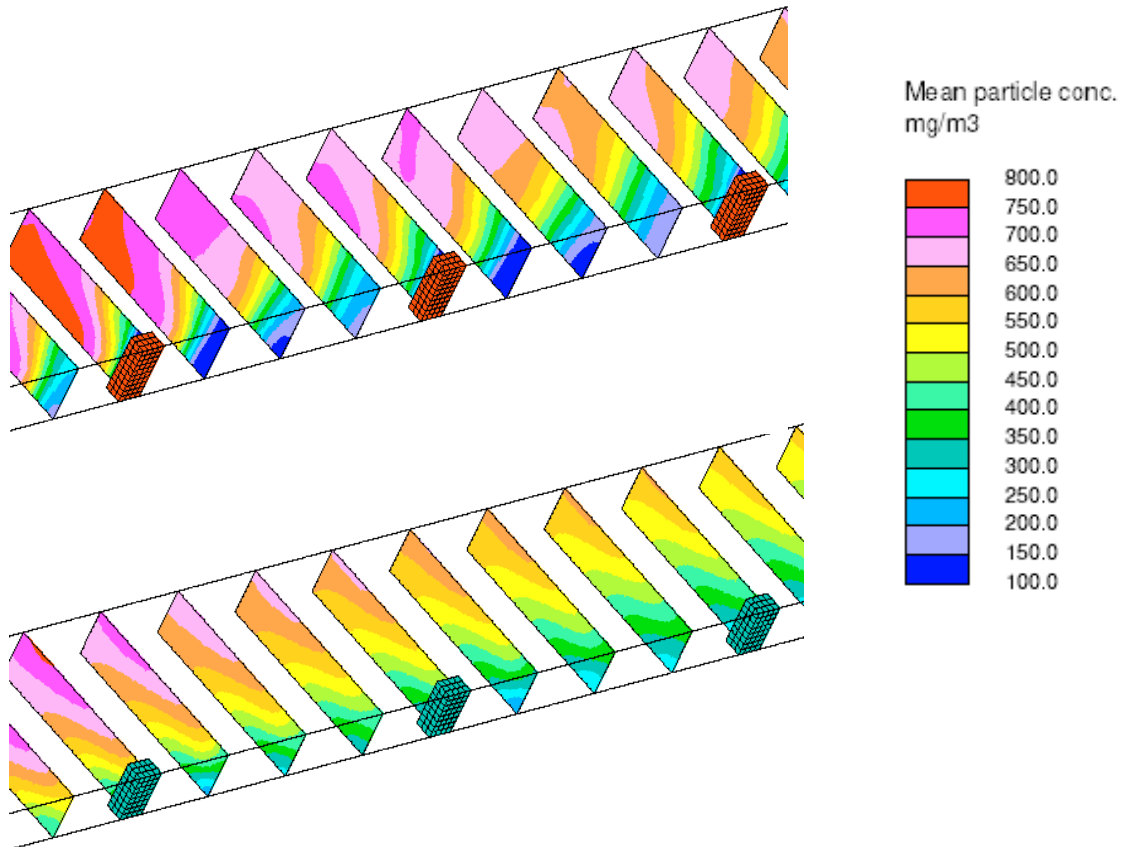


Figure 7. Particle concentration in different axial cross sections for Fibulax-100-0 (upper) and AES-76-0 (lower) electrodes.

Figure 8 demonstrates the secondary flows as velocity vectors and transversal velocity component (iso-colours). In this case a close-up of the flow between the third and the fourth electrode is presented. Notice the clear difference between the secondary flows of the Fibulax-100-0 and AES-76-0 electrode where there is a shift in the flow picture with the staggered electrode (the rolls are waving in the axial direction), while the non-staggered electrode has an almost unchanged roll pattern down through the duct.

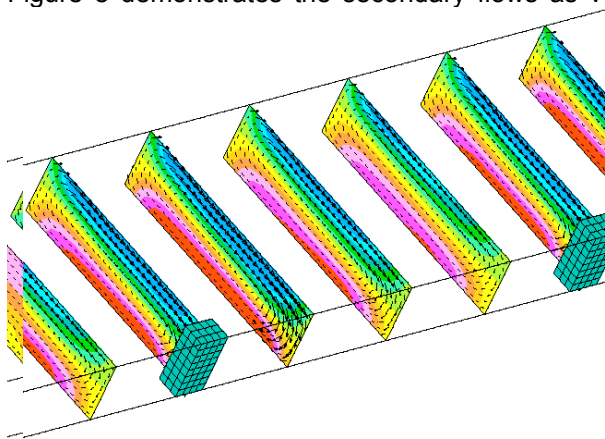


Figure 8. Secondary flows for Fibulax-100-0 electrode at current density of 0.24 mA/m² (left) and for AES-76-0 electrode at current density of 0.30 mA/m² (right).

The plot in Figure 9 shows the current density on the collecting surface for the Fibulax-100-0 electrode at 0.24 mA/m² and for the AES-76-0 electrode at 0.30 mA/m². One electrode quality criterion is the ratio between the area with current density below a certain limit, say 25 μ A/m², and the total collecting area. Another criterion is the ratio between maximum current density and mean current density. Clearly, the non-staggered electrode, is the best in both aspects with an area ratio of 11% as compared to 35% for the staggered electrode and a current density ratio of 2.27 as compared to 3.25 for the staggered electrode.

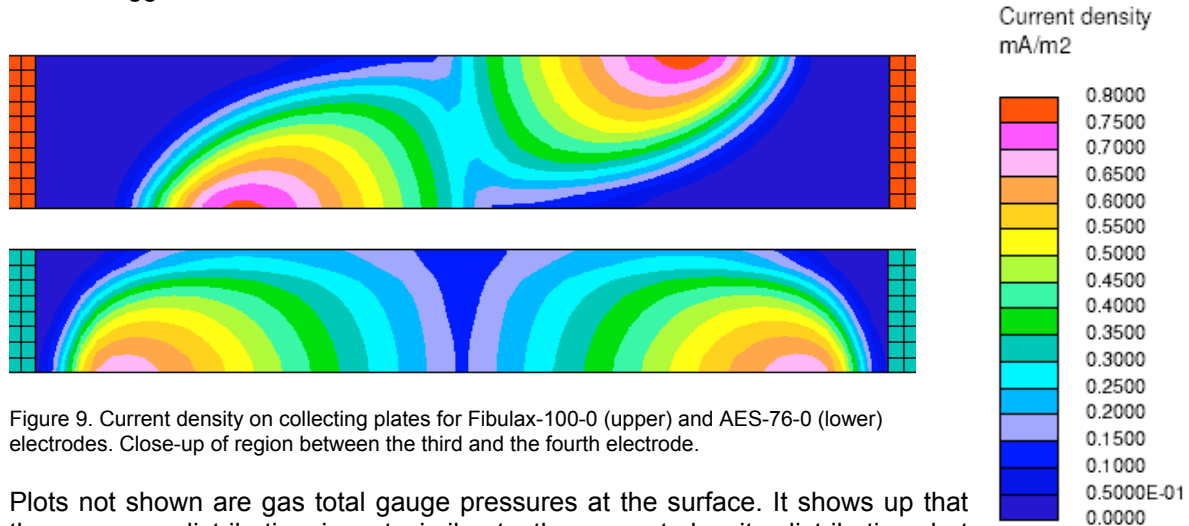


Figure 9. Current density on collecting plates for Fibulax-100-0 (upper) and AES-76-0 (lower) electrodes. Close-up of region between the third and the fourth electrode.

Plots not shown are gas total gauge pressures at the surface. It shows up that the pressure distribution is not similar to the current density distribution, but instead reveals the displacement of the flow due to the electric wind and the dynamic pressure of the flow hitting the wall. The Fibulax-100-0 has a rather uneven total pressure distribution while the AES-76-0 electrode has a more uniform distribution. In both cases the corresponding transport velocity towards the wall can be calculated to unexpected values higher than the transversal roll velocities.

The concentration distribution of dust arriving at the surface is shown in Figure 10. It is well known that the dust pattern shows ellipses of high compactness where the current density is high and areas around the ellipses with low compactness where the current density is low. The staggered Fibulax-100-0 shows a moderate variation of the dust arriving to the surface, about $\pm 13\%$ of average, while the non-staggered AES-76-0 reveals a figure of above $\pm 36\%$. Most remarkable is the difference in the pattern, where the non-staggered electrode creates the highest dust concentration in the upper half of the domain, where the cross flow direction is away from the surface, see Figure 8 right. This is also seen in the areas where the flow direction is away from the surface with the staggered electrode, see Figure 8 left.

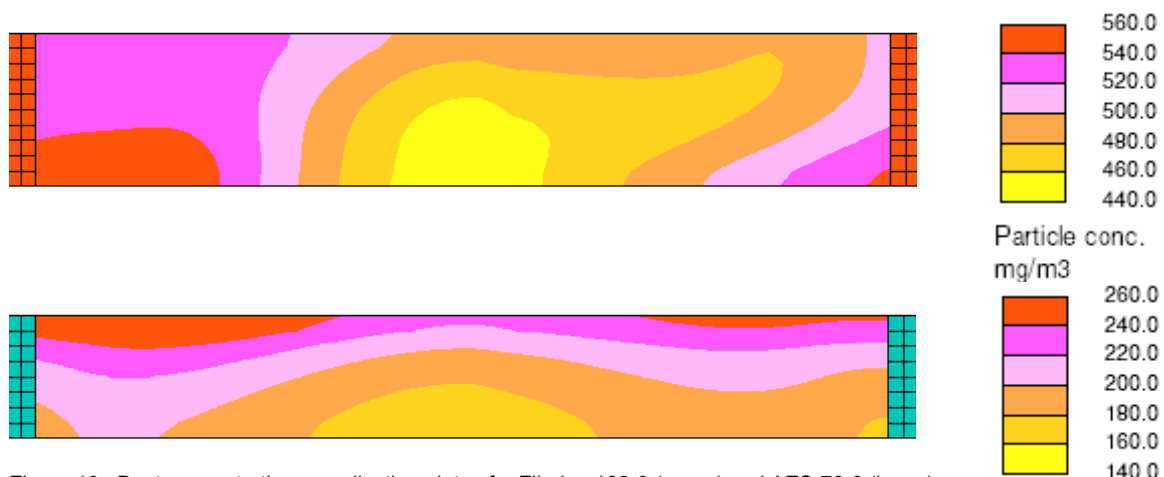


Figure 10. Dust concentration on collecting plates for Fibulax-100-0 (upper) and AES-76-0 (lower) electrodes. Close-up of region between the third and the fourth electrode.

3.3. Case 3 – Influence from current density for AES-76-0 electrode

This section concentrates on field 1 of the pilot ESP set-up with the AES-76-0 non-staggered electrode and investigates the influence from different current density levels.

The quality criteria of area (A_0/A_{tot}) and current density (J_{max}/J_m) ratios defined above is seen in Table 6 for the AES-76-0 electrode at three different current density levels of 0.1, 0.3, and 0.6 mA/m². It is seen that the higher the current density the better the electrode behaves.

| Current density (mA/m ²) | Quality evaluation of AES-76-0 electrode based on different current density levels (A_0/A_{tot}) | J_{max}/J_m is the area where the J_m is less than 25 $\mu\text{A}/\text{m}^2$. |
|--------------------------------------|--|--|
| 0.10 | 21.0% | 2.45 |
| 0.30 | 10.5% | 2.27 |
| 0.60 | 8.9% | 2.18 |

The plots of Figure 11 demonstrate the secondary flows for three mean current densities, 0.10, 0.30, and 0.60 mA/m². The higher the current density is, the more intense

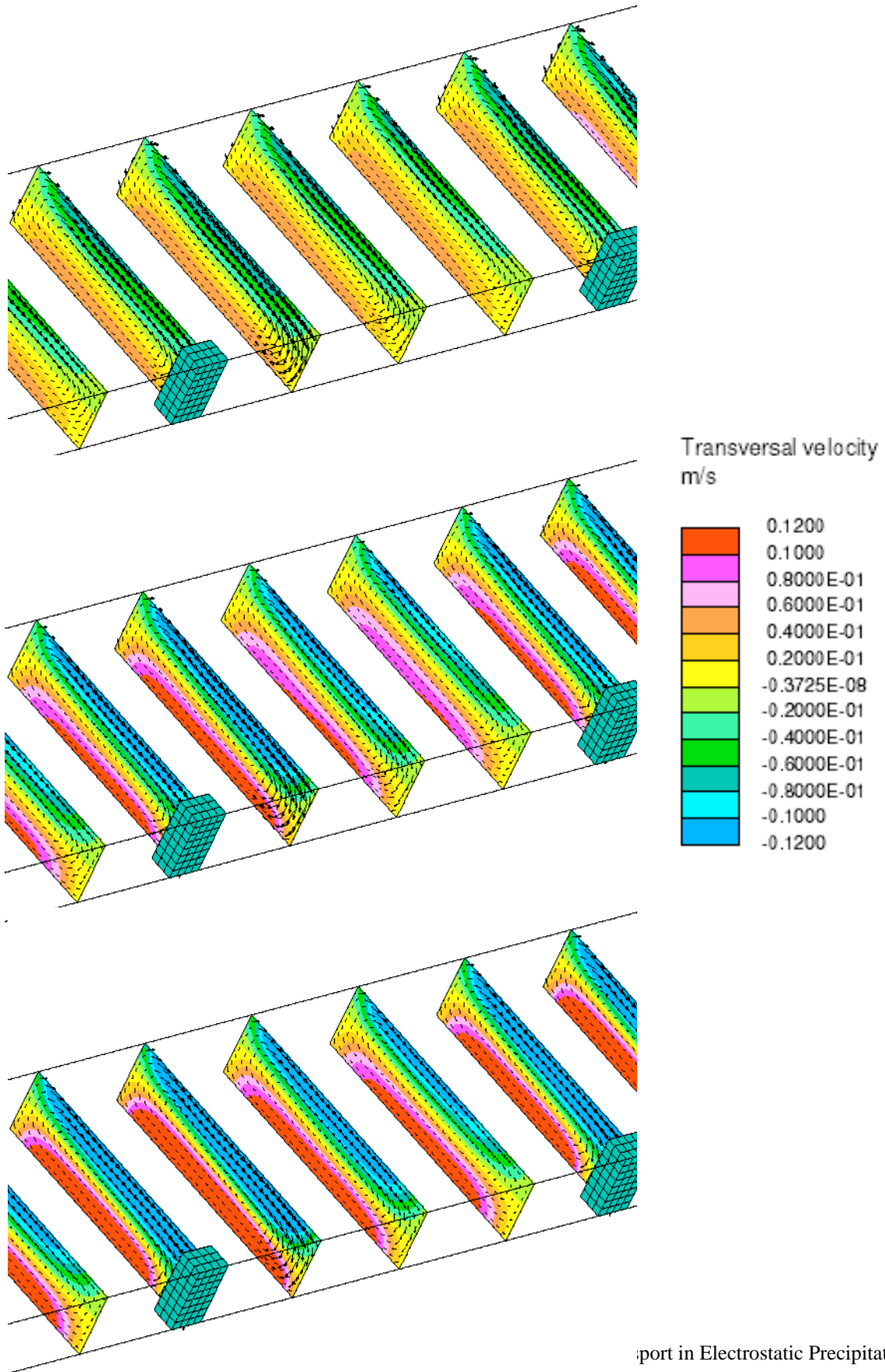


Figure 11. Secondary flows for three current density levels of 0.1 (upper), 0.3 (middle), and 0.6 mA/m² (lower). The figure shows the transversal velocity component as well as velocity vectors.

the secondary flow becomes and it is noteworthy that the roll picture is almost unaltered.

The plots in Figure 12 show examples of electric field distributions: ^{a)} to the left and right in a transverse plane containing the discharge electrode, ^{b)} in the center in an axial symmetry plane between two neighbouring electrodes, and ^{c)} perpendicular to these planes a field distribution at the collecting surface. The courses of the fields perpendicular to the plate surface are as expected ^{a)} from electrode corona field strength to 2.47 kV/cm at the plate, and ^{b)} from zero at the mid-plane to 2.27 kV/cm at the plate surface. The plate field is rather constant, 2.3 - 2.5 and only small regions above 2.5 kV/cm compared to a nominal field strength of 2.5 kV/cm = voltage divided by half duct width.

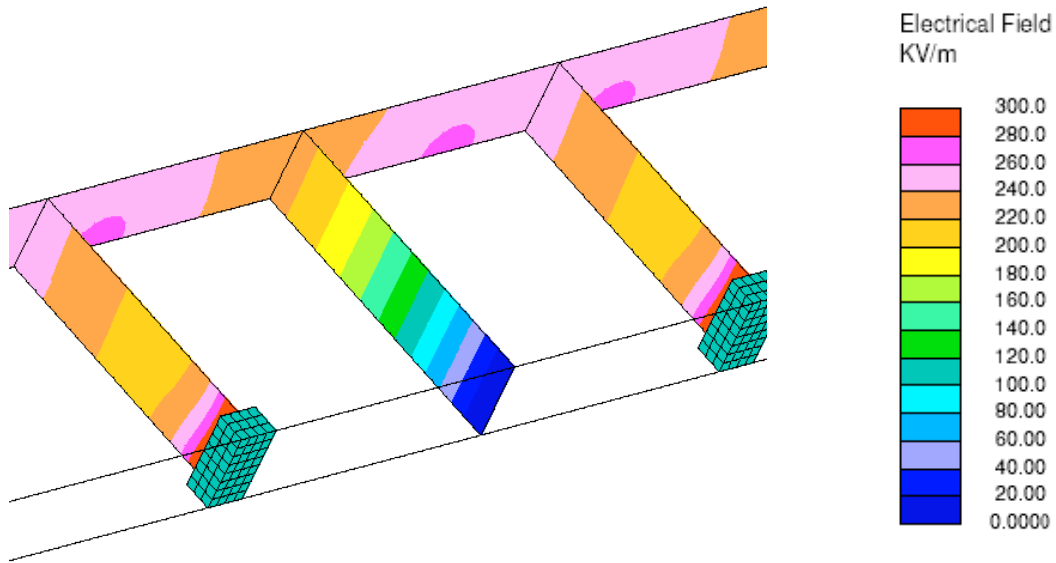


Figure 12. Electric field at different axial cross sections between third and fourth electrode and at the collecting plate for a current density level of 0.3 mA/m².

In Figure 13 the ionic and dust space charges for different current densities are shown for the AES-76-0 electrode. The moderate increase in ionic space charge reveals a slightly increasing current with axial length. The decrease in particle (dust) space charge is due to the change in particle concentration through the precipitator, and at the inlet the dust space charge increases less than proportional to the mean current density.

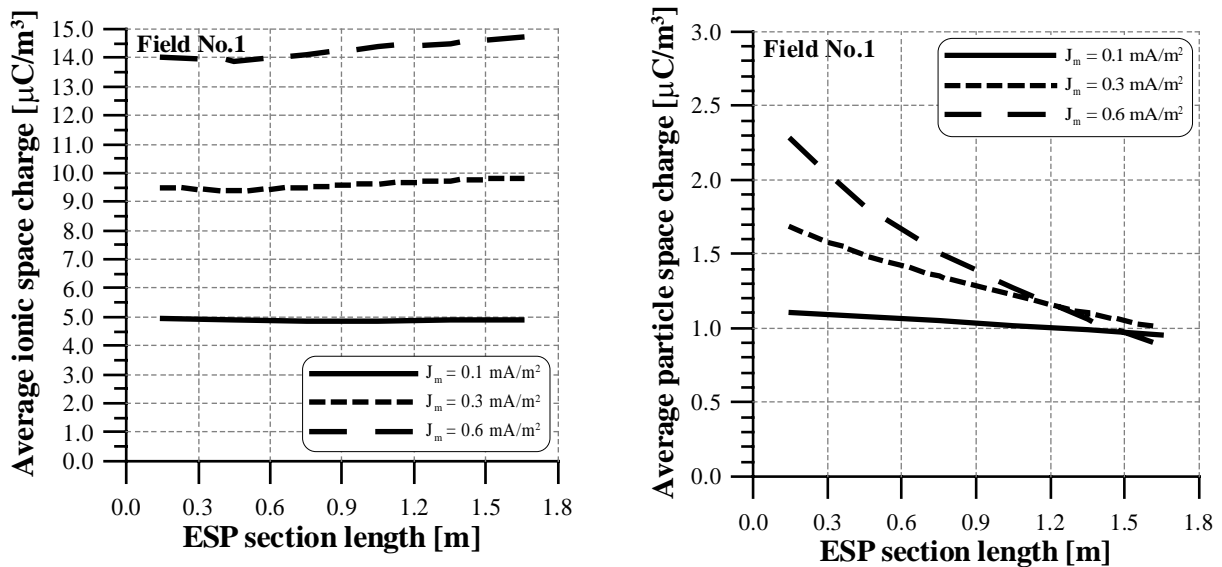


Figure 13. Left graph shows the calculated ionic space charge, and the right graph shows the particle space charge along the precipitator, both at 0.1, 0.3, and 0.60 mA/m². AES-76-0 electrode.

4. Conclusions

The present paper highlights parameters important for optimal ESP performance and shows the capabilities of the new FLS Airtech simulation model to predict parameters that cannot be measured in the field or even in a laboratory pilot model set-up.

The model is able of describing the secondary rolls physically correct and has the further advance of pre and post-processing being much easier due to the graphical interface of the commercial code.

It has been demonstrated that the code can predict the ESP efficiency well in case of a commercial precipitator with relative coarse dust, while there is quite some discrepancy trying to calculate the emission measured on a pilot precipitator working with fine dust and low inlet loading.

The code can easily calculate the current distribution, secondary flow pattern, and space charge of new discharge electrodes provided the corona starting voltage is known for a clean electrode under laboratory conditions.

In near future an improved diffusion charging model will be included in order to be able to predict the ESP operation with fine particles. E.g. a sinter plant Dry ESP (DESP) or a Wet ESP (WESP) with high droplet space charges. Special interest is on the ability of a given electrode to operate with proper voltages and current densities without sparking or quenching.

References

- Akoh, E. & Nielsen, N.F., 2000, EFP-2000: Electrostatic Precipitation – Reduction of Emission and Energy Consumption, Software Specification, FORCE Technology (formerly DMI) report: TN.2000878, FORCE Technology, Lyngby, Denmark.
- Anagnostopoulos, J., Bergeles, G.C., 2002, Corona discharge simulation in wire-duct electrostatic precipitator, *J Electrostat* 54, p.129-147.
- Arrondel, V., Bacchiega, G., Gallimberti, I., ESP Modelling: From University Studies to Industrial Application, Proceedings of 8th. International Conference on Electrostatic Precipitation, May. 14-17, 2001, Birmingham, Alabama, USA, Session A4-2.
- Egli, W. Kogelschatz, U. & Persson, T., Three-Dimensional Corona Current Distribution in Complex ESP Configurations, Proceedings of 6th. International Conference on Electrostatic Precipitation, June 18-21, 1996, Budapest, Hungary, pp.166-171.
- Ferziger, J. H. & Peric, M., 1996, Computational Methods for Fluid Dynamics, Springer.
- Houlgreave, J.A., Bromley, K.S. & Fothergill, J.C., A Finite Element Method for Modelling 3D Field and Current Distribution in Electrostatic Precipitators with Electrodes of Any Shape, Proceedings of 6th. International Conference on Electrostatic Precipitation, June 18-21, 1996, Budapest, Hungary, pp.154-159.
- Lauder, B.E., and Spalding, D.B., 1974, The numerical computation of turbulent flow, *Comp. Meth. in Appl. Mech. & Eng.*, 3, p. 269.
- Lawless, P.A., 1996, ESPVI 4.0 Electrostatic Precipitator V-I Performance Model - User's Manual. Center for Aerosol Technology, Research Triangle Institute, North Carolina, USA.
- Medlin, A.J., Fletcher, C.A.J. & Morrow, R., Electrohydrodynamic Modelling of Fine Particle Collection in Electrostatic Precipitators, Proceedings of 7th. International Conference on Electrostatic Precipitation, Sept. 20-25, 1998, Kyongju, Korea, pp.665-672.
- Meroth, A.M., Nicolaus, S., Levin, P.L. & Schwab, A.J., Effective Solution of 3D Charge Coupled Problems in Electrostatic Precipitators, Proceedings of 6th. International Conference on Electrostatic Precipitation, June 18-21, 1996, Budapest, Hungary, pp.137-143.
- Parasram, N.R., Taylor, A.M.K.P., 2001, Particle motion in electrostatic precipitators, Proceedings of 8th, International Conference on Electrostatic Precipitation, May. 14-17, 2001, Birmingham, Alabama, USA, Session A1-2.
- Schmid, H.-J. & Buggisch, H., On the Modelling of Particle Transport in Electrostatic Precipitators, Proceedings of 7th. International Conference on Electrostatic Precipitation, Sept. 20-25, 1998, Kyongju, Korea, pp.673-687.
- Schmitz, W., Gibson, D. & Pretorius, L., Computational Fluid Dynamics Modelling of Collection Dynamics, Proceedings of 8th. International Conference on Electrostatic Precipitation, May. 14-17, 2001, Birmingham, Alabama, USA, Session A2-1.
- Southern Research Institute, 1975, A mathematical model of Electrostatic Precipitation, Southern Research Institute, PB 246 188, April 1975.
- STAR-CD manual, version 3.15, 2001, Computational Dynamics Ltd., London, UK.
- Thomsen HP; Larsen PS; Christensen EM; Christiansen JV (1982) Velocity and turbulence fields in negative corona wire-plate precipitator. Fourth Symp. on the Transfer and Utilization of Particulate Control Technology, Houston, Texas, 1982 (II, p.243, EPA-600/9-025 b, Nov.1984).
- Wilcox, D.C. 1993, Turbulence Modeling for CFD, DCW Industries, Inc., California, USA.
- Zamany, J., 1992, Modelling of particle transport in Commercial Electrostatic Precipitators, Ph.D Thesis, ATV EF 316, Technical University of Denmark and FLS Airtech A/S (formerly FLS miljø a/s).
- Zamany, J., 1995a, Numerical modeling of electrodynamic conditions influenced by particle space charge and resistivity in electrostatic precipitators of complex geometry for industrial applications, *Inst Phys Conf Ser No 143*: 357-362.

Zamany, J., 1995b, Numerical modeling of electrodynamic conditions influenced by particle space charge and resistivity in electrostatic precipitators of complex geometry for industrial applications, FLS Airtech A/S (formerly FLS miljø) Internal report, FLS Airtech, Valby, Denmark.